Zentrum für Technomathematik

Fachbereich 3 – Mathematik und Informatik

3D Finite element simulation of a material accumulation process including phase transitions and a capillary surface

M. Jahn **A. Schmidt**

E. Bänsch

Report 14–01

Berichte aus der Technomathematik

Report 14–03 **December 2014**

3D FINITE ELEMENT SIMULATION OF A MATERIAL ACCUMULATION PROCESS INCLUDING PHASE TRANSITIONS AND A CAPILLARY SURFACE

M. JAHN, A. SCHMIDT, AND E. BÄNSCH

Abstract. In this article, a 3D finite element simulation of a material accumulation process based on rod end and blank end melting is discussed. This process represents the first step of a two-level cold forming process in micro-range and can be modeled mathematically by coupling the Stefan problem with the Navier-Stokes equations including a free capillary surface. Numerical results for melting the tip of a wire and a thin metal blank end plain as well as the accumulation of material along a pierced blank are presented.

1. Introduction

In advanced engineering, the importance of micro-components has increased significantly during the last decade. Unfortunately, methods used in macro-scale are sometimes no longer applicable to very small work-pieces, so the need for new methods and processes arises.

A classical forming process, visualized in Figure 1.1, is a characteristic example for a process where miniaturization, i. e. using the same approach for metallic micro-components, leads to problems such as bending. Due to this, the Collaborative Research Center 747 "Micro Cold Forming" developed a two-level cold forming process for metallic components in micro-range which takes advantage of size effects [17], namely, the shape-balance effect, due to the fact that in micro range surface tension exceeds gravitational force. The two-level cold forming process, visualized in Figure 1.2 [2, 3] for thin metal rods, is described in various papers, e. g. [13, 16, 18]. A laser heat source is either coaxially or laterally applied to the workpiece and melts the material. The shape-balance effect causes the melt to form an almost perfect sphere that solidifies after the laser is switched off. The generated preform is then calibrated in a subsequent forming step in a open die. By using the two-level cold forming process upset ratios $s := \frac{l_0}{d_0} >> 200$ can be reached while the conventional process is limited by the value $s = 2.1$ and decreased, if d_0

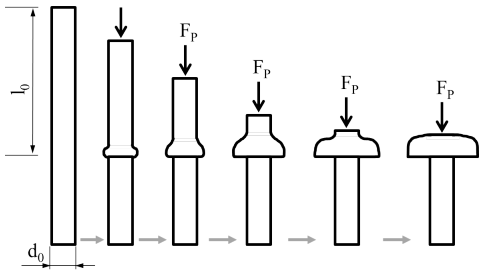

Figure 1.1. Conventional multilevel cold forming process in macro range

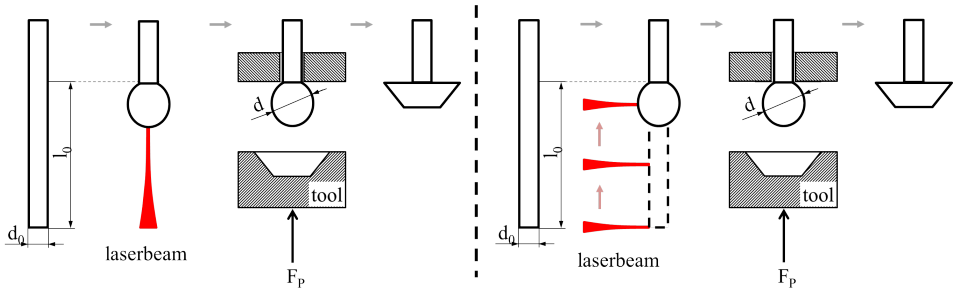

FIGURE 1.2. Two-level cold forming process used by SFB 747 with coaxial applied laser heat source (left) and lateral applied laser heat source (right) in the material accumulation step

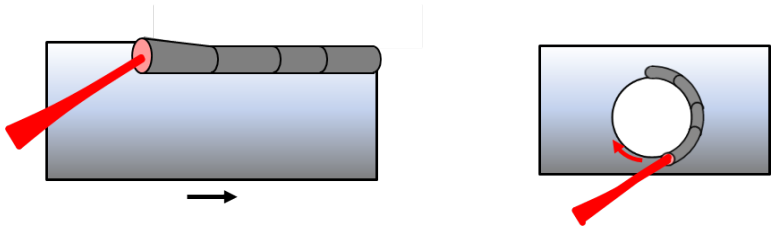

FIGURE 1.3. Preform generation at a blank end plain (left) and a pierced blank (right)

does. The material accumulation step described above can also be used to generate preforms at blank end plains or pieced blanks as shown in Figure 1.3.

For analyzing the process and to determine process parameters, the material accumulation process is simulated numerically. Therefore, we model the first step of the two-level cold forming process by coupling the Stefan problem with the Navier-Stokes equations including a free capillary surface, cf. [5, 6].

For the numerical solution of the coupled problem, one can choose between several approaches e.g. an implicit method based on the enthalpy model [1] and an explicit approach using a sharp interface model [6]. Both methods have their pros and cons so one has to choose a appropriate method according to the application.

In our previous work, the material accumulation process was studied for coaxially irradiated work-pieces. For melting the tip of a rod, a 2D rotational symmetric approach as been used. Therefore, we developed a numerical method which bases on a combination of both, implicit and explicit methods [12]. In order to simulate the generation of preforms at blank end plains, a 2D cross section model has been developed using a heat source as a right-hand-side in the heat equation to include heat transport orthogonal to the laser direction [11].

However, a full 3D simulation is needed to simulate the material accumulation process for more general situations such as lateral irradiation of work-pieces or more complex geometries such as pierced blanks. This paper presents such a method based on the enthalpy-approach.

2. MATHEMATICAL MODEL

The modeling of a melting and solidification process needs to consider the energy balance in the work-piece and the dynamics in the melt. The energy balance

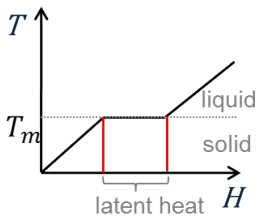

FIGURE 2.1. Temperature-enthalpy relation

dependents on laser heating, heat transport, radiation described by the Stefan-Boltzmann law, forced convection and phase transitions. All those effects can be modeled by the two-phase Stefan problem in enthalpy formulation [7, 14] with appropriate boundary conditions. To include the dynamics in the melt, the incompressible Navier-Stokes equations with a free capillary surface [4] are used. By applying additionally boundary conditions and suitable volume forces, effects like buoyancy effect and Marangoni convection can be taken into account.

Combining both problems into one model leads to a coupled system of partial differential equations that can be solved numerically by using a finite element method. The full mathematical model as it is used in this paper is published in e. g. [9, 12].

2.1. **Enthalpy model.** For our application, we adapt the Stefan problem in enthalpy formulation to a formulation including thermal convection. Then the energy balance in the time-dependent domain $\Omega(t)$ is given by

$$\partial_t H + u\nabla H - \frac{1}{\mathrm{RePr}}\Delta T = 0 \quad \text{in } \Omega(t), \tag{2.1}$$

with $u \equiv 0$ in $\Omega_s(t)$ and

$$T = \alpha(H) := \begin{cases} \frac{\rho_s c_{p_s}}{\rho_l c_{p_l}} H, & H < 0 \\ 0, & H \in \left[0, \frac{1}{\mathrm{Ste}}\right] \\ H - \frac{1}{\mathrm{Ste}}, & H \geq \frac{1}{\mathrm{Ste}} \end{cases} \tag{2.2}$$

describing the temperature-enthalpy relation where H and T denotes the enthalpy resp. the temperature. Thereby, the temperature is scaled so that melting temperature corresponds to the zero level, i.e. $T_{melt} = 0$. Ste is the Stefan number and the ratio $\frac{1}{\mathrm{Ste}}$ defines the latent heat. The coefficients ρ and c_p denote the density and the specific heat capacity in the liquid resp. solid subdomain. Equation (2.2) is visualized in Figure 2.1. By solving equation (2.1) with appropriate boundary conditions as named above, the solid-liquid interface $\Gamma_S(t) := \{x \in \Omega(t) | T(x) = 0\}$ is given implicitly and, therefore, can naturally handle the nucleation and the vanishing of a liquid subdomain as well as multiple solid-liquid interfaces or a mushy region.

3. NUMERICAL METHOD

The coupled system is solved numerically by using an implementation of a solver for the Stefan problem in enthalpy formulation that has been integrated in the finite element solver NAVIER [4].

3.1. **Navier.** The finite element software NAVIER has been developed for solving flow problems with free capillary surfaces, on time-dependent domains discretized by unstructured tetrahedral grids. The Navier-Stokes equations are discretized by the Taylor-Hood element in space, i.e. piecewise quadratics for the velocities and

piecewise linears for the pressure and the capillary surface is handled by using a semi-implicit, variational treatment of the curvature terms in the Navier-Stokes equations. For time discretization the fractional-step θ scheme in an operator splitting variant is applied [1], so the flow problem is decoupled from the geometry deformation.

3.2. **Stefan problem in enthalpy formulation.** The enthalpy FE method basing on the enthalpy model treats phase transitions implicitly and, therefore, is very flexible. Linear elements are used for the discretization and the interface $\Gamma_S(t)$ is obtained by interpolation of the temperature and, in general, not given on element edges but intersects elements. In regards to the coupling of the Stefan problem with the flow problem and especially the capillary surface, we need a method to handle these intersected elements in the numerical simulation. The most simple way is to consider an element as "solid" for the flow problem as long as it is intersected by $\Gamma_S(t)$. By doing so, one avoid discontinuities within elements. Another approach which can be used is based on remeshing: After every time step one can create a new mesh that aligns with the interface and the capillary surface. Unfortunately, remeshing is numerically very expensive, especially in 3D.

There are many more approaches to handle intersected elements which are omitted here. Instead, we use the simple approach to show some results that can be obtained by solving the coupled PDE system.

4. Results

Using the presented method, we are able to 3D simulate melting and solidification processes with a capillary surface. Our application is a material accumulation process in which a laser heat source, see Table 2 for the specifications, is applied to a thin wire or a thin blank of austenitic chromium nickel steel 1.4301 whose material parameters are given in Table 1. The rod end melting and blank end melting processes are methods to create preforms which are upset in an open die to generate functional micro-components as described in the introduction.

Table 1. Material properties of steel 1.4301 (X5CrNi18-10) [15] resp. iron[1] [8]

T_0	293 K	initial temperature
T_a	293 K	ambiance temperature
T_m	1673 K	melting temperature
ρ	7900 kg/m^3	density
c_{p_s}	500 J/kg K	specific heat capacity in solid
c_{p_l}	830 J/kg K	specific heat capacity in melt
λ_s	15 J/mK	thermal conductivity in solid
λ_l	35 J/mK	thermal conductivity in melt
H_M	276000 J/kg	latent heat
μ^1	$5.5 \cdot 10^{-3}$ Ns/m^2	dynamic viscosity
γ^1	1.872 N/m	surface tension
β^1	10^{-4} 1/K	coefficient of thermal expansion
α_L	0.38	absorption coefficient

TABLE 2. Specifications of the laser system

Laser	Trumpf TruFiber 300
Laser type	Fibre laser
Wavelength	1085 nm
Focal distance	100 mm
Beam radius	0.02 mm
Divergence angle	40 mrad

4.1. **Generation of preforms at rods.** The generation of preforms at rods using a coaxially applied laser source is analyzed in various papers, e. g. [2, 9, 10, 16, 18]. For the numerical studies, a 2D rotational symmetric approach [6, 12] can be used for a coaxially applied laser heat source. In case of a laterally applied heat source, a full 3D model has to be used for simulating the material accumulation process.

Experimental setup. The experiments performed by our cooperation partner BIAS are carried out using rods with initial diameters d_0 between 0.1 mm to 0.5 mm as wrought material. The laser beam is placed laterally to the rod surface, and is deflected accordingly to the movement of the interface $\Gamma_S(t)$ along the symmetrical axis of the rod, cf. Fig. 4.1.

Simulation results. When applying the laser beam laterally to the surface of the rod, the material melts with a solid-liquid interface $\Gamma_S(t)$ that is inclined in laser direction, see Figure 4.3a. This inclination angle of $\Gamma_S(t)$ depends on the process parameters, especially the deflection velocity of the laser beam alongside the rod and the laser power. As a consequence of the inclined interface, the melt drop is eccentric during the process, cf. Figure 4.3b.

After the laser is switched off, there is still excess energy in the material that allows for further melting of material. During this intermediate process, the heat transport in the melt leads to a decrease in the inclination angle and consequently the eccentricity of the melt drop, as visualized in Figure 4.3c. Ideally, the preform is centrically when the preform cools down and solidifies, see Figure 4.3d.

Energy balance. The energy dissipation of laser rod melting has been analyzed and quantified for the heating period of the process, if the laser is coaxially applied to the rod [9]. It turned out that the radiation is the most important mechanism reducing the efficiency of the material accumulation process. We compare the heat

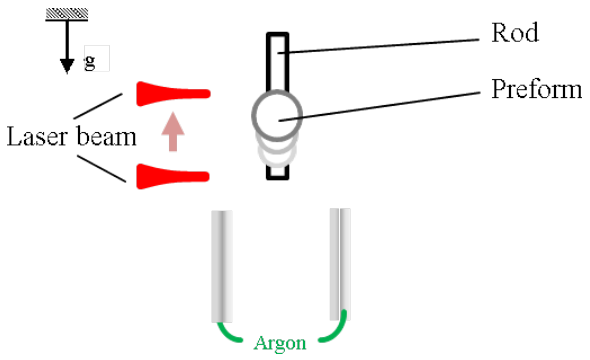

FIGURE 4.1. Experimental setup for the material accumulation process step

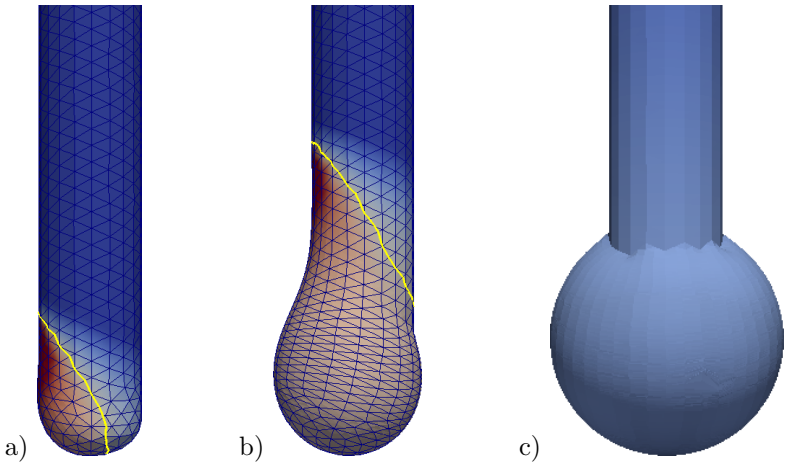

FIGURE 4.2. Material accumulation process on rods using a laterally applied laser beam

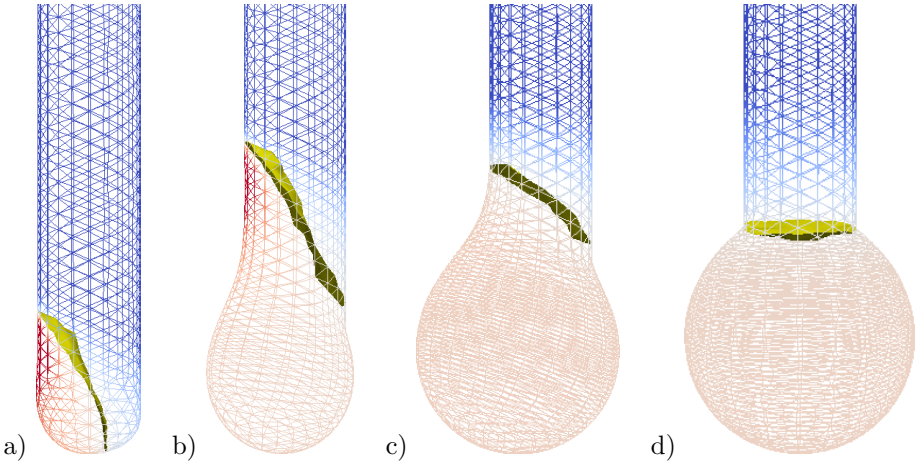

FIGURE 4.3. Material accumulation process on rods using a laterally applied laser beam

TABLE 3. Process parameters

Rod diameter	0.4 mm
Power	129 W
Pulse duration	100 ms
Shielding gas	argon
Shielding gas temperature T_{SG}	293 K
Shielding gas velocity	200 $\frac{\mathrm{W}}{\mathrm{m^2 K}}$
Deflection velocity	30 $\frac{\mathrm{mm}}{\mathrm{s}}$

fluxes resulting from a coaxially applied heat source to the fluxes that occur, if a laterally applied laser beam is used. The process parameters are given in Table 3.

In Figure 4.4, the heat fluxes arising from a coaxially applied laser heat source are shown, including laser heating, radiation and the forced convection due to shield

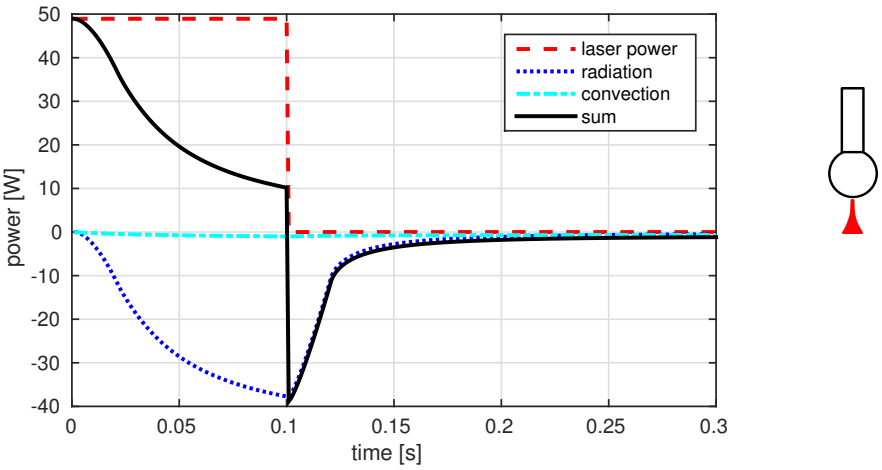

FIGURE 4.4. Energy flux in melting process with coaxially applied laser beamm

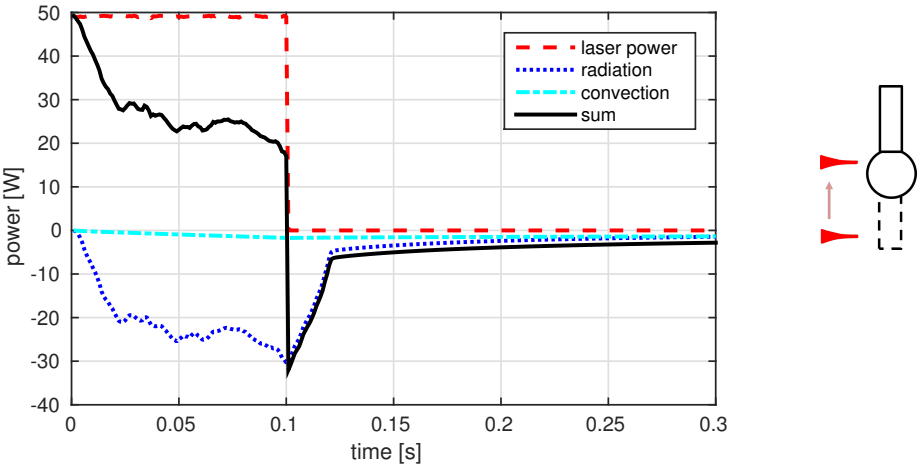

FIGURE 4.5. Energy flux in melting process with laterally applied laser beam

gas cooling. It can be seen that during the heating period, the material absorbs constantly 49 W[1]. During the melting process, the heat losses due to radiation and convection increase permanently reducing thereby the energy available for the accumulation process, as indicated by the graph "total". At $t = 0.1$ s, only round about 10 W can be actually used for the melting whereas approximately 39 W are lost due to radiation and forced convection. After the laser is switched off at $t = 0.1$ s, the work-piece has absorbed 4.9 J in total. Approximately 2.87 J of this amount of energy are dissipated due to radiation and convection.

In the same way, the heat fluxes generated by a laterally applied laser beam are visualized in Figure 4.5. As before, effectively 49 W are constantly applied to the rod during the irradiation time $t = 0.1$ s. The heat source is deflected along the rod with a velocity of 30 mm/s. Similar to the energy fluxes considered for coaxial laser heating, the amount of energy that can actually be used for the melting process

[1]The applied laser energy is $P = 129$ W and the absorption coefficient is $\alpha = 0.38$, cf. Table 1

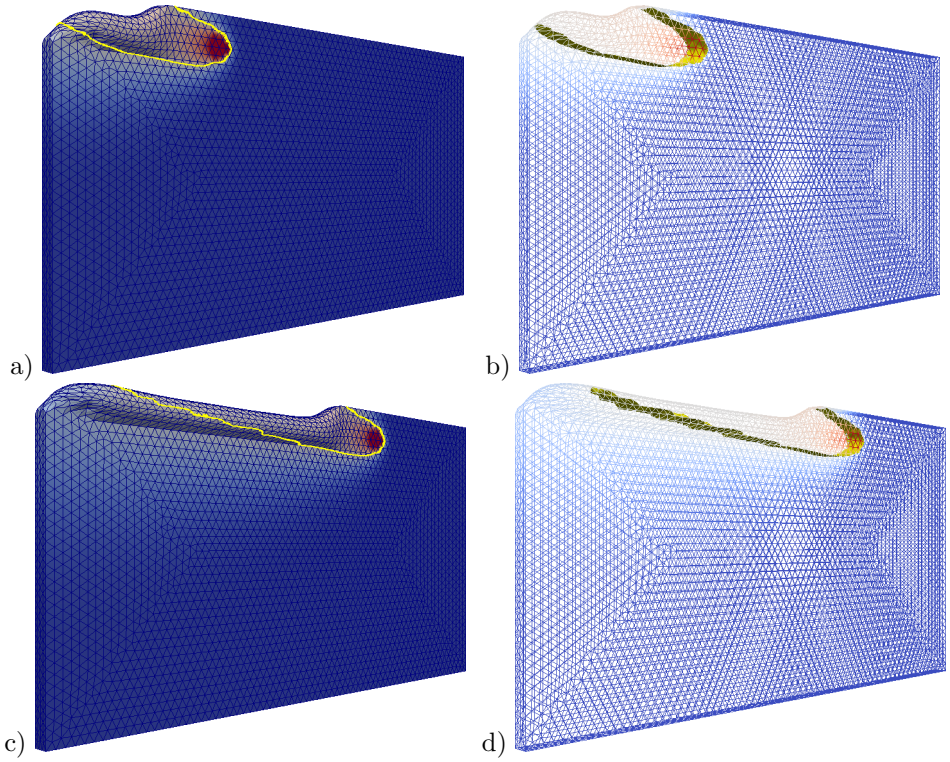

FIGURE 4.6. Preform generation at blank end plains: A laterally applied laser heat source melts the material that forms a collar

decreases during the process to approximately 19 W at $t = 0.1$ s. In total, round about 2.49 J of the absorbed energy are dissipated by radiation and convection.

Comparing both figures, it can bee seen that the fluxes for a laterally applied heat source align qualitatively with the results for coaxially laser rod melting and with [9]. However, the heat losses arising due to radiation and convection are quantitatively with approximately 2.49 J significantly less then the dissipated 2.87 J that arise, if the laser beam is coaxially applied to the rod, making the process using laterally irradiation much more effective. The reason for this is that for a coaxially applied laser beam, the heat has to be transported from the tip work-piece trough the whole melt. By doing so, the temperature in the melt and, consequently, the amount of energy that is dissipated due to radiation and convection increases significantly in comparison to the laser rod melting process using a laterally applied heat source.

In summary, the efficiency of laser rod melting can be considerably increased, if the heat source is laterally applied to the rod and deflected alongside the symmetry axis of the rod instead of using a coaxially irradiation.

4.2. **Generation of preforms at blanks.** The material accumulation process can also be used to generate thermal preforms at blank end plains and pierced blanks. In contrast to the generation of preforms at rods, this process is hardly analyzed. In the following, some first simulation results are presented.

Experimental setup. The thickness of the blanks for the process can be varied between 50 μm and 300 μm. For the pierced blank, the diameters of the void is typically varied between 0.5 mm and 1 mm. In both setups, the laser beam is placed laterally to the blank's surface and is deflected as shown in Figure 1.3.

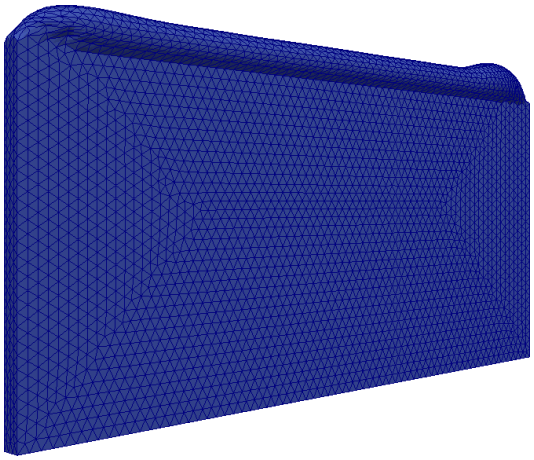

FIGURE 4.7. Thermal preform at blank end plain

TABLE 4. Process parameters for preform generation at blank end plains

Blank thickness	0.15 mm
Laser offset	0.6 mm
Power	290 W
Pulse duration	100 ms
Shield gas	argon
Shield gas temp. T_{SG}	293 K
Shield gas velocity	200 $\frac{\mathrm{W}}{\mathrm{m^2K}}$
Deflection velocity	30 $\frac{\mathrm{mm}}{\mathrm{s}}$

TABLE 5. Process parameters for preform generation at pierced blanks

Blank thickness	0.15 mm
Laser offset	0.1 mm
Void diameter	0.75 mm
Power	46 W
Shield gas	argon
Shield gas temp. T_{SG}	293 K
Shield gas velocity	200 $\frac{\mathrm{W}}{\mathrm{m^2K}}$
Deflection velocity	41 $\frac{\mathrm{mm}}{\mathrm{s}}$

Simulation results for preform generation at blanks. The simulation results for laser blank melting alongside a blank end plain are obtained by using the parameters given in Table 4 and for generating a preform at a pierced blank, the parameters presented in Table 5 are used.

Firstly, a laser heat source is deflected alongside a blank end plain and melts the material. Surface tension and gravity force the melt to form a collar at the blank end, see Figure 4.6, This shape is preserved after the heat source is switched off and the melt is solidified, cf. in Figure 4.7.

In the next example, a blank is pierced so that it contains a cylindrical void. A laterally applied heat source is deflected along a circular path in small distance, the so called "offset", to the void, see Figure 4.8. As before, the material melts and forms a collar around the void. After switching off the laser, the shape of the collar is preserved and a closed preform is generated as shown in Figure 4.9.

5. CONCLUSIONS

A full 3D finite element simulation of a material accumulation process based on rod end melting as well as blank end melting is presented. Numerical results for thermal preform generation at rods and blanks are given. By comparing laterally and coaxially applied heat sources, it can be seen that by using laterally applied laser heat source, the efficiency of the process can by considerably increased.

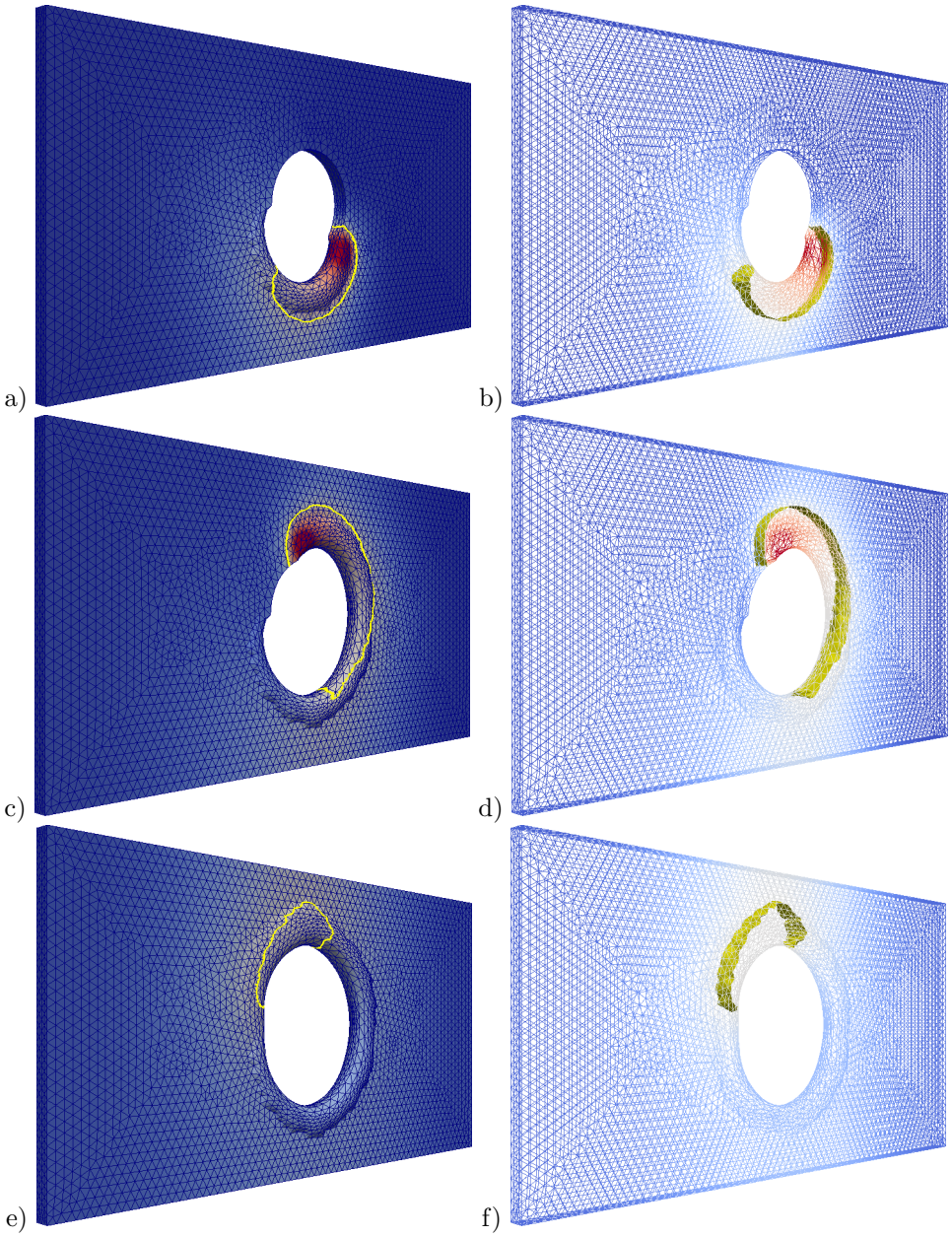

FIGURE 4.8. Energy flux in melting process with laterally applied laser beam

ACKNOWLEDGEMENT

The authors gratefully acknowledge the financial support by the DFG (German Research Foundation) for the subproject A3 within the Collaborative Research Center SFB 747 “Mikrokaltumformen - Prozesse, Charakterisierung, Optimierung”. Furthermore, we thank the Bremer Institut für angewandte Strahltechnik (BIAS) for cooperation.

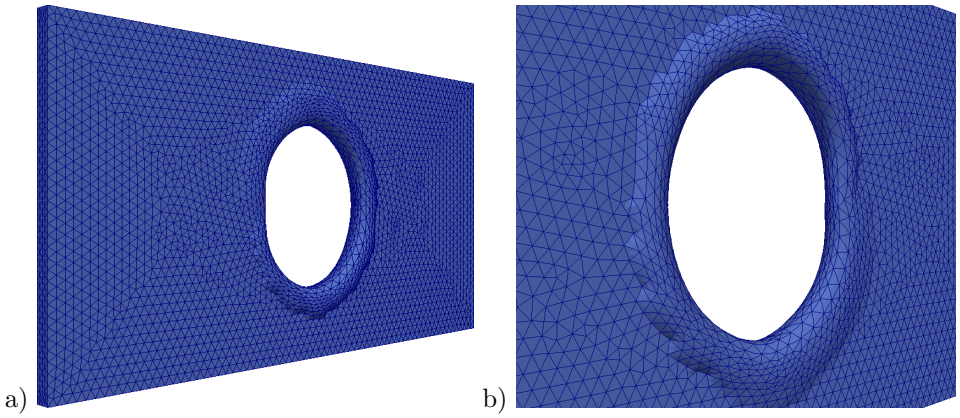

FIGURE 4.9. Closed thermal preform at pierced blank

REFERENCES

[1] M. O. Bristeau, R. Glowinski, and J. Periaux. Numerical methods for the Navier-Stokes equations. Application to the simulation of compressible and incompressible flows. *Computer Physics Report*, 6:73–188, 1987.

[2] H. Brüning, M. Teepe, and F. Vollertsen. Surface roughness and size effect in dendrite arm spacing at preforms of aisi 304 (1.4301) generated by laser rod end melting. *Procedia Engineering*, 81(0):1589 – 1594, 2014. 11th International Conference on Technology of Plasticity, ICTP 2014, 19-24 October 2014, Nagoya Congress Center, Nagoya, Japan.

[3] H. Brüning and F. Vollertsen. Self-aligning capability of laser based free form heading process. In *Proceedings of 11th International Scientific Conference MMA - Advanced Production Technologies*, 2012.

[4] E. Bänsch. Finite element discretization of the Navier-Stokes equations with a free capillary surface. *Numerische Mathematik*, 88(2):203–235, 2001.

[5] E. Bänsch, J. Paul, and A. Schmidt. An ALE FEM for solid-liquid phase transitions with free melt surface. Technical Report 10-07, ZeTeM, Bremen, 2010.

[6] E. Bänsch, J. Paul, and A. Schmidt. An ALE finite element method for a coupled Stefan problem and Navier–Stokes equations with free capillary surface. *International Journal for Numerical Methods in Fluids*, 2012.

[7] C. M. Elliot. On the finite element approximation of an elliptic variational inequality arising from an implicit time discretization of the Stefan problem. *IMA Journal of Numerical analysis*, 1:115–125, 1981.

[8] W.F. Gale and T.C. Totemeier. *Smithells Metals Reference Book*. Elsevier Science, 2003.

[9] M. Jahn, H. Brüning, A. Schmidt, and F. Vollertsen. Energy dissipation in laser-based free form heading: a numerical approach. *Production Engineering*, 8(1-2):51–61, 2014.

[10] M. Jahn, A. Luttmann, and A. Schmidt. A FEM simulation for solid-liquid-solid phase transitions during the production of micro-components. In *Proceedings of 11th International Scientific Conference MMA - Advanced Production Technologies*, 2012.

[11] M. Jahn, A. Luttmann, and A. Schmidt. Finite element simulation for material accumulation and welding processes including a free melt surface. *PAMM*, 13(1):235–236, 2013.

[12] M. Jahn, A. Luttmann, A. Schmidt, and J. Paul. Finite element methods for problems with solid-liquid-solid phase transitions and free melt surface. *PAMM*, 12(1):403–404, 2012.

[13] T. Kokalj, J. Klemenčič, P. Mužič, I. Grabec, and E. Govekar. Analysis of the laser droplet formation process. *Journal of Manufacturing Science and Engineering*, 128(1):307–314, 2006.

[14] L. I. Rubinštejn. *The Stefan Problem*, volume 27 of *Translations of Mathematical Monographs*. American Mathematical Society, Rhode Island, 1971.

[15] Lamineries MATTHEY SA. Stahl 1.4301. Technical Report 2013/01, Lamineries MATTHEY SA, Lamineries MATTHEY SA, CH-2520 La Neuveville, 2013.

[16] A. Stephen and F. Vollertsen. Influence of the rod diameter on the upset ratio in laser-based free form heading. *Steel Research Int., Special Edition: 10th Int. Conf. on Technology of Plasticity (ICTP)*, pages 220–223, 2011.

[17] F. Vollertsen. Categories of size effects. *Prod. Eng.-Res. Dev. 2*, pages 377–383, 2008.

[18] F. Vollertsen and R. Walther. Energy balance in laser based free form heading. *CIRP Annals*, 57:291–294, 2008.

The Center for Industrial Mathematics, University of Bremen, 28359 Bremen
E-mail address: mischa@math.uni-bremen.de

The Center for Industrial Mathematics, University of Bremen, 28359 Bremen
E-mail address: schmidt@math.uni-bremen.de

Applied Mathematics III, University Erlangen–Nürnberg, 91058 Erlangen
E-mail address: eberhard.baensch@math.fau.de